Shape-induced translational mode transition and self-entrapment of self-propelled metallodielectric rods

Iwashita, Yasutaka
Department of Physics, Kyoto Sangyo University

Kimura, Yasuyuki
Department of Physics, Kyushu University

出版情報：Physical Review E. 113 (5), pp.L053404-, 2026-05-19. American Physical Society (APS)
バージョン：

Shape-Induced Translational Mode Transition and Self-Entrapment of Self-Propelled Metallodielectric Rods

Yasutaka Iwashita,[1,*] and Yasuyuki Kimura[2]
[1]Department of Physics, Kyoto Sangyo University, Kyoto 603-8555, Japan
[2]Department of Physics, Kyushu University, Fukuoka 819-0395, Japan

ABSTRACT. We study the self-propulsive motion of Janus rectangular rods with high aspect ratios (≥ 5), emphasizing the influence of morphological anisotropy on their dynamics. These metallodielectric rods self-propel *via* induced-charge electrophoresis (ICEP), moving perpendicular to their long axis. The pronounced anisotropic shape gives rise to distinct behaviors, including a discontinuous transition in translational mode, self-entrapment at small obstacles, and self-excited oscillations when trapped. Our findings highlight the pivotal role of shape in determining the motion and interactions of micro-scale active agents, with implications for the design and control of active matter systems and microengineered devices.

I. INTRODUCTION

Recent advances in particle synthesis have enabled the fabrication of diverse artificial microswimmers [1,2], offering unconventional approaches and new insights across multiple research fields. As smart microrobots, these microswimmers can transport and manipulate materials in microfluidic devices and MEMS systems [3,4]. In contrast to biological active agents such as microorganisms and animals, artificial microswimmers are physically and chemically well-defined and designable, making them versatile tools for fundamental studies in active matter [1,2,5-7].

For self-propulsion to occur, symmetry breaking is essential to establish a preferred direction of motion. Geometric anisotropy such as particle shape or patchy surface structure is often central to this process [1,8,9]. Shape also plays a crucial role in interparticle interactions such as hard body interactions, thereby linking it directly to both single-particle dynamics and collective behavior of microswimmers. Simulations by Moran *et al*. demonstrate that active Brownian particles with polygonal shapes exhibit rich nonequilibrium phase behaviors, including side-number-dependent motility-induced phase separation [10,11]. Shape also plays a key role in biological active matter; for instance, crawling cells self-propel *via* contact forces with a substrate, where cell shape strongly influences force generation [12]. Experimental work has also highlighted the role of shape in active agents [13-18], though such works remain relatively limited compared with theoretical and computational investigations.

Here, we investigate how shape influences the self-propulsive behavior of an artificial microswimmer fabricated by photolithography [19,20], focusing on pronounced *uniaxial* anisotropy. The microswimmer is self-propelled by induced-charge electrophoresis (ICEP) [21-23], a propulsion mechanism well-suited for synthetic particles. ICEP utilizes electrical and/or morphological anisotropy of particles under applied DC or AC electric fields, offering precise control over propulsion through the field strength. Under AC fields, our swimmers translate perpendicular to their long axis. This propulsion direction contrasts sharply with that of agents in active nematics, a well-studied class of active matter systems [24-27]. In active nematics, elongated swimmers propel along their long axis, and the alignment between shape and propulsion direction is central to the emergence of nematic order and collective nonequilibrium behavior.

We show that this simple yet highly anisotropic design gives rise to several distinctive behaviors. These include sideways propulsion of vertically oriented rods driven by torque balance, spontaneous shape-induced entrapment at small obstacles, and self-excited oscillations under entrapment. These results demonstrate an intriguing coupling between swimmer geometry and force balance, highlighting how anisotropic shape can generate dynamical states not accessible in weakly anisotropic or spherical systems.

II. METHODS

Our swimmer is a metallodielectric Janus rectangular rod composed of an epoxy-based resin (SU-8) with a 25-nm-thick chromium (Cr) layer deposited on one width-length face (Fig. 1a). Unless otherwise noted, the rod width is fixed at $w = 2.0\ \mu\text{m} \pm 2\%$ (coefficient of variation), and the height is $h = 1.4\ \mu\text{m} \pm 20\%$. The rod length l ranged from 5.0 to 80.0 μm ±2%, corresponding to aspect ratios (l/w) between 2 and 40 (Figs.1c-e). The rods were dispersed in a 0.1 mM aqueous NaCl solution and

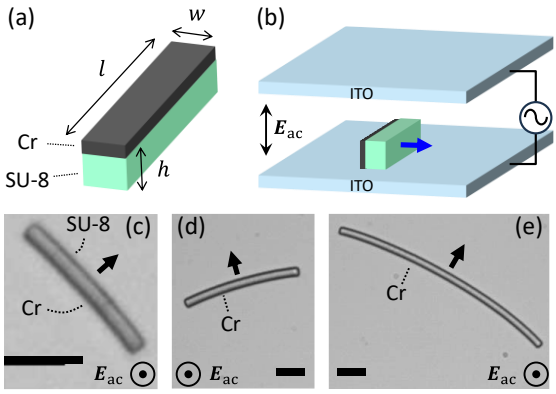

FIG 1. Samples. (a) Schematic of the rod geometry and dimensions. The Cr layer is shown in dark gray and the SU-8 body in green. (b) Schematic of experimental setup. (c-e) Optical microscopy images of dispersed rods with $l = 20, 40$, and 80 μm, respectively. Longer rods in (d) and (e) exhibit slight bending toward the Cr-coated side. Thick arrows indicate the direction of ICEP motion. Scale bars: 10 μm.

sedimented to the bottom of the sample cell (Fig. 1b) [28].

To induce ICEP, we applied a square-wave AC voltage at a frequency $f = 1$ kHz, orienting perpendicular to the bottom plane of the cell. The applied electric field strength was $V_p/100$ [V/μm], where V_p [V] is the voltage amplitude and 100 μm is the spacing between the ITO electrodes confining the rod dispersion [28].

III. RESULTS AND DISCUSSIONS

A. V_p-dependence of translational motion.

We first describe the behavior of rods with length $l = 40$ μm as a representative case. Before voltage application, the rods were randomly oriented with respect to their Cr-coated face, while their long axis remained parallel to the bottom plane. As V_p gradually increased from zero, rods with their Cr face oriented either upward or downward rotated by 90° around their long axis at a small V_p (~0.1 V), aligning the Cr face perpendicular to the bottom plane. At this point, the rods initiated self-propulsion *via* ICEP. They translated in the direction of the SU-8 side, with velocity perpendicular to their long axis (Fig. 2a, left).

In different from Janus spheres, the rods exhibited a discontinuous change in translational behavior at higher voltages. At a critical $V_p (\equiv V_p^{up} = 1.6$ V, corresponding to $V_p^2 = 2.56$ V^2 in Fig. 2b), the rods abruptly reoriented to stand upright, with their long axis aligned normal to the bottom plane [28]. During this transition, one end lifted off the substrate and moved faster than the other end, which remained in contact with the substrate (Fig. 2a, center). After reorientation, the rods continued ICEP propulsion. We refer to the state with the rod lying parallel to the bottom plane as the *horizontal mode* and the upright state as the *vertical mode*. Hereafter, the translational speed v is defined as the steady-state value measured more than 10 s after changing V_p, which is independent of the voltage history (Fig. S1 [28]).

The speed–voltage relation in Fig. 2b shows a clear discontinuity in v and pronounced hysteresis. In both modes, $v \propto V_p^2$, consistent with previous studies [22,23]. Upon decreasing V_p after the transition to the vertical mode, the rod returned to the horizontal mode at a lower threshold ($V_p^{down} = 1.0$ V $< V_p^{up}$), accompanied by an increase in speed. The $v - V_p$ plots for rods with $l = 10, 20, 40$, and 80 μm in Fig. 2c further demonstrate the length dependence: both the magnitude of the speed change at the mode transition and the hysteresis width ($V_p^{up} - V_p^{down}$) increase with l.

The trend of speed change becomes more pronounced in Fig. 2d (see Fig. S2 for V_p^{up} and V_p^{down} [28]). To compare the translational speeds in Fig. 2c, we plot the proportionality constant $k_i = v/V_p^2$, where i = h and v denote the horizontal and vertical mode, respectively. As shown, k_h increases from ~1 to 3 μm/V^{2}s with increasing l and appears to saturate around l~40 μm. In contrast, k_v decreases markedly with l, from ~1 to 0.2 μm/V^{2}s. Accordingly, the ratio k_v/k_h decreases monotonically with rod length, reaching 0.07 at $l = 80$ μm (Fig. S2b [28]), highlighting the growing disparity between the two propulsion modes.

To address the origin of the hysteresis, we qualitatively analyze the rod's orientation in terms of the torques arising from gravitational, electric, and induced-charge electroosmotic (ICEO) effects. We assume the rod behaves as a conductor, since the electrical response of the metallic layer (chromium) is much stronger than that of the dielectric body (SU-8). Consider a thin rod of length l and effective mass m in an electrolyte solution, where m is defined as the product of the rod-solution density difference and the rod volume. Under an externally applied electric field of strength E, the rod experiences two types of torques: an electric torque resulting from the induced electric dipole moment and a hydrodynamic torque generated by the surrounding ICEO flow. Both act to align the rod parallel to the electric field [32, 33]. When an AC electric field is applied, the magnitudes of these torques depend on the frequency. However, their dependences on E and the rod-field angle $\theta (0 \leq \theta \leq \pi/2)$ are identical, allowing the combined torque

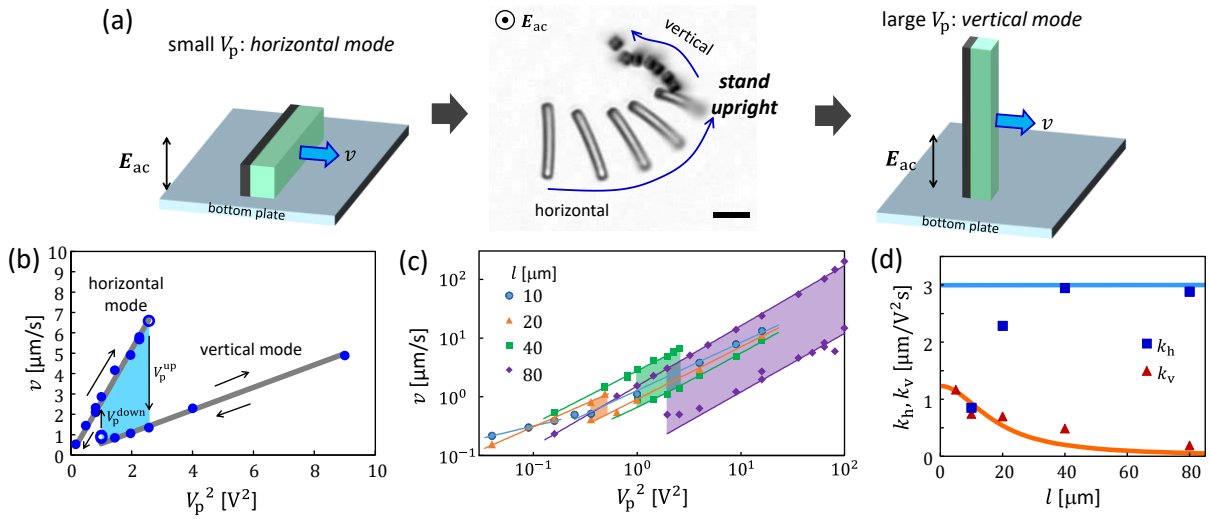

FIG 2. V_p-dependence of translational modes. (a) Schematic of the translational mode transition. The left and right panels correspond to the horizontal and vertical modes, respectively. The center panel shows an overlaid microscopy image (8 s interval, ImageJ "Z Project" [29]) of a rod with $l = 20$ μm at $V_p = 0.8$ V (see Movie 1 [28]). Scale bar: 10 μm. (b) Translational speed v as a function of ${V_p}^2$ for a rod with $l = 40$ μm. Arrows indicate the direction of changes for increasing ($0.0 \rightarrow 3.0$) and decreasing ($3.0 \rightarrow 0.0$) V_p. Gray lines represent linear fits for each mode. Filled circles denote translational states that remained stable for ≥ 50 s. Open circles denote unstable states that transitioned within 50 s, with speeds measured prior to transition. Data were collected over multiple cycles between the two modes. (c) V_p-dependence of v for rods with $l = 10$ (blue circles), 20 (orange triangles), 40 (green squares), and 80 μm (purple diamonds). The data for $l = 40$ μm are identical to (b). For all length except $l = 10$ μm, the upper and lower branches correspond to the horizontal and vertical modes, respectively. For $l = 10$ μm, $V_p^{up} \cong V_p^{down} \cong 0.45$ V; the left branch (${V_p}^2 < 0.2$ V^2) corresponds to the horizontal mode and the right (${V_p}^2 > 0.2$ V^2) to the vertical mode. Data were obtained over multiple cycles between the two modes. (d) Proportionality constant k_h and k_v for the horizontal and vertical modes, respectively. Each point represents the average over several rods (standard deviation ~30%). k_v is calculated from speeds at particular V_p between 2 and 4 V, while k_h includes values obtained from linear fit of v vs. ${V_p}^2$. The curve with k_v shows the fitted theoretical relation, $k_v \propto \frac{1}{1+\omega^2\tau_p^2}$ [21, 28]. The line $k_h = 3.0\ \mu$m/V^{2}s is derived from the analytical solution for a cylindrical rod [22].

to be expressed as $N_e = -\alpha E^2 \sin\theta\cos\theta$, where α is a positive constant. The gravitational torque, acting to align the rod horizontally when one end is in contact with the bottom surface, is given by $N_g = \frac{1}{2}mgl\sin\theta$, where g is the gravitational acceleration and the electric field is applied normal to the horizontal plane. In the viscous limit, the angular velocity of the rod satisfies

$$\zeta\dot{\theta} = N_g + N_e = \alpha E^2 \sin\theta\,(k - \cos\theta)\,, \qquad (1)$$

where ζ is the viscous coefficient for rotation and $k = \frac{mgl}{2\alpha E^2} \equiv (E_c/E)^2$.

Equation (1) qualitatively explains the observed bistability. When the electric field is weak ($E \le E_c$), $k \ge 1$, and thus $\dot{\theta} > 0$ except $\theta = \pi/2$ (and $\theta = 0$ when $k = 1$), making the horizontal orientation ($\theta = \pi/2$) the only stable state. When the electric field strength increases beyond E_c, $k < 1$, leading to two stable orientations. For $\cos\theta < k$, $\dot{\theta} > 0$, and θ increases toward $\pi/2$, corresponding to horizontal orientation. For $\cos\theta > k$, $\dot{\theta} < 0$, and θ decreases toward 0, corresponding to the vertical orientation. With further increases in E, k approaches zero, rendering the horizontal orientation unstable; the rod then switches to the vertical orientation in response to small perturbations such as thermal fluctuations or slight heterogeneities in the rods and substrate. When E decreases back, the vertical orientation becomes unstable as k sufficiently approaches unity, and the rod returns to the horizontal orientation. This asymmetry in the k values for the orientational transitions accounts for the difference in the electric field strengths (or voltages) required for the forward and reverse transitions. This simple model is for explaining the hysteresis, but not the length

dependence of the orientational transition. Incorporating the l-dependence of the electric field–induced torques into this framework is nontrivial, as discussed later.

We next analyze the speed in the two translational modes within the framework of ICEP theory. The two modes—horizontal and vertical—correspond to distinct electrokinetic flow around the rod, and thus possibly to different ICEP propulsion mechanisms.

In the horizontal mode, the speed agrees with the analytical expression for a symmetric metallodielectric Janus cylinder of infinite length aligning perpendicular to the applied electric field. The speed is given by $v = \frac{4}{3\pi}\frac{\varepsilon a}{\eta(1+\delta)}E^2$, where η is the viscosity, ε the dielectric permittivity, a the cylinder radius, and δ the ratio of the compact- to diffuse-layer differential capacitances [22, 23]. This yields $k_\mathrm{h} = 3.0\ \mu\mathrm{m/V^2s}$, shown as the horizontal line in Fig. 2d [28]. The asymptotic behavior of the experimental k_h toward this analytical value with increasing rod length likely reflects the diminishing influence of finite-length effects in longer rods. While the agreement is qualitative rather than quantitative owing to differences in rod geometry and boundary conditions (bulk vs. nearby a substrate), it nonetheless supports the relevance of ICEP theory to our system.

In the vertical mode, however, the induced surface charge is localized around the rod ends [32], and finite length must therefore be considered. To our knowledge, no closed-form analytical expression exists for this geometry. Instead, we discuss the length dependence of the speed using the electro-osmotic slip velocity u_s, assuming $v \propto u_\mathrm{s}$. In ICEP/ICEO theory, $u_\mathrm{s} \sim U_0 = \frac{\varepsilon E^2 l}{2\eta}$ [21, 22]. Under AC powering, the time-averaged slip velocity contains frequency-dependent factor, $\frac{1}{1+\omega^2\tau_\mathrm{p}^2}$, where $\omega = 2\pi f$ and $\tau_\mathrm{p} = \lambda l/2D$ with λ the Debye screening length, D the diffusion constant, and τ_p the RC charging time for EDL formation against the induced surface charge [21]. These lead to $k_\mathrm{v} \propto \frac{l}{1+\omega^2\tau_\mathrm{p}^2}$ [34]. Experimentally, however, the observed l-dependence of k_v is better captured by the charging-time term alone, $1/(1+\omega^2\tau_\mathrm{p}^2)$ (Fig. 2d) [28], suggesting that U_0 becomes effectively independent of l. Such independence can be attributed to the saturation of slip velocity with particle size. Indeed, Gangwal *et al*. [23] reported that the speed of metallodielectric Janus spheres increases linearly with diameter d for small d, whereas it becomes nearly constant for $d \gtrsim 10\ \mu\mathrm{m}$ under conditions comparable to ours. Since most of our rods are in this size range, such saturation can explain why the vertical-mode speed depends primarily on charging time rather than rod length.

It is worth noting the size dependence of the EDL formation time, $\tau_\mathrm{p} = \lambda x/2D$, where x is the characteristic length parallel to the electric field. For our rod dimensions, the maximum τ_p^{-1} is 55 kHz $\gg f$ in the horizontal mode ($x = w = 2\ \mu\mathrm{m}$), and the minimum τ_p^{-1} is 1.4 kHz $\approx f$ in the vertical mode of $x = l = 80\ \mu\mathrm{m}$ rod [28]; i.e., $f \lesssim \tau_\mathrm{p}^{-1}$ for all rod lengths and orientations examined. In addition, the RC charging time of the cell, τ_cell, is estimated as $\tau_\mathrm{cell}^{-1} = 1.1\ \mathrm{kHz} \approx f$ for $x = 100\ \mu\mathrm{m}$, indicating that the applied electric field itself is partially screened by the EDL on the ITO electrodes.

These results demonstrate that competition between electric-field-induced and gravitational torques can produce strongly nonlinear translational behavior, owing to their distinct dependences on field strength and rod length. Notably, gravity, typically a minor factor in microswimmer dynamics [1, 2], is substantially amplified by the large aspect ratio. The observed dynamics further suggest the possibility of multistep transitions between translational modes in swimmers with multi-axis anisotropy, either in the conducting region or in the overall shape.

Finally in this section, we discuss the effect of large induced potentials. Gangwal *et al*. [23] attributed velocity saturation to large induced surface potentials, with $\zeta_\mathrm{i} = Ed/2 \cong 10\ V_\mathrm{th}$ for $d = 8\ \mu\mathrm{m}$, where $V_\mathrm{th} = k_\mathrm{B}T/e = 26$ mV is the thermal voltage, k_B is the Boltzmann constant and e is the elementary charge. The slip-velocity scale U_0 and the standard ICEP/ICEO theory assume small surface potentials ($\zeta_\mathrm{i} \lesssim V_\mathrm{th}$) and dilute electrolytes [21, 22], so ζ_i of this magnitude is large enough to necessitate nonlinear corrections [21, 35, 36]. In our experiment, $\zeta_\mathrm{i} = El/2$ is two orders of magnitude larger than V_th for the vertical mode of $l = 80\ \mu\mathrm{m}$ rods, suggesting remarkable nonlinear effect. Nonetheless, our results show that $v \propto E^2 (\propto {V_\mathrm{p}}^2)$, consistent with the standard theory, even for $l = 80\ \mu\mathrm{m}$ (Fig. 2c). Although smaller exponents than 2 are generally expected and observed under such conditions [34, 35-37], the persistence of quadratic scaling suggests that the effective induced surface potential may be orders of magnitude smaller than $\zeta_\mathrm{i} = Ed/2$, as proposed previously and supported by the correction factor $1/(1+\delta)$ for our experiment [34, 35-37].

We return here to the length dependence of the orientational transition. The proposed suppression of the scaling of U_0 with l would modify the functional form of the field-induced torque N_e, and consequently its length dependence, particularly at small θ. Moreover, although the ICEO torque is expected to dominate over the electric dipolar torque for our rod lengths ($f \lesssim \tau_\mathrm{p}^{-1}$ [32, 33]), a reduction in the effective surface potential would weaken the ICEO

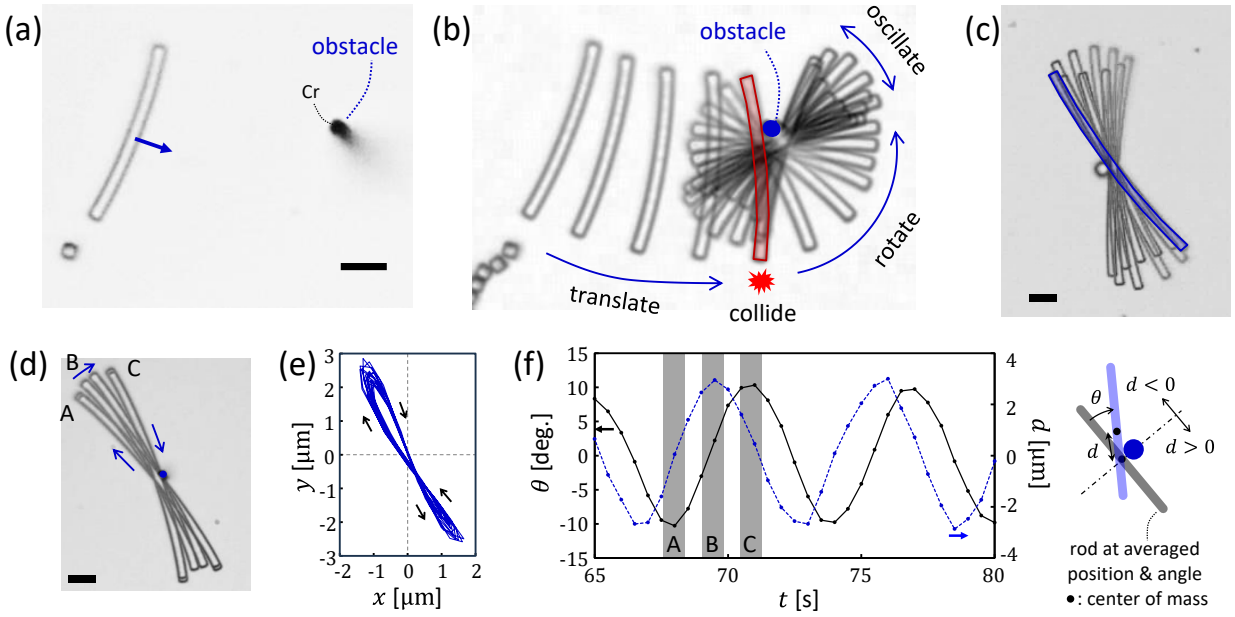

FIG 3. Self-entrapment and self-excited oscillation of horizontal mode rods. (a-d) Microscopy images. Panels (b) and (c) are overlaid images (4s intervals). (a) An $l = 40$ μm rod approaches a small obstacle, here a rod vertically adhered to the substrate. (b) The rod in (a) exhibits rotation and oscillation upon collision [28]. (c) Oscillation of an $l = 80$ μm rod around a cylindrical SU-8 micropillar with 4.0 μm diameter [28]. (d) Overlaid image of the oscillating $l = 80$ μm rod, corresponding to the time regions labeled in (f) [28]; the same rod as in Fig. S5a [28]. (e) Trajectory of the rod's center of mass over ~16 oscillation cycles, corresponding to the rod in (d). The origin, $(x, y) = (0,0)$, is defined as the time-averaged position over the cycles (in 150 s). The trajectory shows slight asymmetry. (f) Time evolution of the angle θ (black dots and solid line) and the signed distance d of the rod's center from the origin (blue dots and dashed line), corresponding to the rod in (d). $t = 0$ marks the time when V_p is changed. A schematic illustrates the definitions of θ and d. Applied voltages: $V_p = 1.0$ V for (a) and (b); 2.0 V for (c); and 4.0 V for (d-f). Scale bars: 10 μm.

contribution and could alter this balance. For $\theta \sim \pi/2$, the rectangular and asymmetric Janus geometry should be treated explicitly to obtaining accurate torques, rather than the thin-conductor approximation. Hydrodynamic effects associated with horizontal translation nearby a substrate should also be incorporated for a more complete description [38].

As discussed above, clarifying the role of nonlinear effects in the observed dynamics remains an important direction for future work.

B. Self-entrapment of horizontal-mode rods by small obstacles.

We report the behavior of long rods ($l = 40$ and 80 μm) in the horizontal mode upon collision with small obstacles. When a rod collides off-center with an obstacle, it initially undergoes rotation and substantially begins to oscillate as its center comes close to the obstacle (Figs. 3a, 3b, and S5a [28]). This behavior was observed for two types of obstacles: a dielectric SU-8 micropillar fabricated by photolithography (Fig. 3c) and a vertically oriented rod that had accidentally adhered to the bottom substrate (Figs. 3a, 3b and S5a [28]).

This phenomenon can be understood as self-entrapment of the rod by the obstacle, explained by a simple force-balance argument. Since the rods possess a thin metal layer along their entire length, they generate self-propulsive forces perpendicular to their long axis at every point along their length. Upon off-center collision with an obstacle, the resulting asymmetry in force distribution produces a torque that drives rotation, causing the "longer arm" of the rod to move forward (Fig. 3b, counterclockwise rotation). As the rotation proceeds and the rod's center approaches the obstacle, the torque gradually diminishes. Once the center aligns with the obstacle, the propulsive forces balance on both sides, halting the rotation.

In active matter systems, accumulation or entrapment of active agents in geometrically distinct regions (e.g., wall corners) is well established [1]. Our findings reveal that even simple uniaxial anisotropy can induce geometric entrapment through their own propulsion, even against point-like obstacles.

The oscillation that follows the initial rotation is a self-excited oscillation of the self-propulsive rod. Such oscillatory behavior is typically observed in passive systems driven by external energy sources; here, however, the rod itself acts as a nonequilibrium open system. The rod tip traces an elliptical trajectory (Fig. 3c and S5a [28]), indicating that the oscillation involves both translational displacement and angler variation. Figures 3d-f show the temporal evolution of the rod's orientation and center of mass. The center of mass follows a slender figure-eight trajectory (Fig. 3e). Figure 3f presents time series data of the rod's angle θ and the *signed* distance d of its center of mass from the origin. Here, θ is defined as the clockwise angle, with the 150 s time-averaged orientation set to $\theta = 0°$. d is defined as $\mathrm{sign}(x-y) \times \sqrt{x^2+y^2}$, such that $d < 0$ in the top-left quadrant and $d > 0$ in the bottom-right quadrant of Fig. 3e. A clear phase difference between θ and d is evident in Fig. 3f. Figure 3d shows overlaid images of the rod at three representative time regions labeled A, B, and C in Fig. 3f. When angular motion ceases (region A), variations in d are pronounced, and the rod extends toward the top-left, as indicated by the sign reversal of d. The asymmetry in arm lengths relative to the obstacle generates torque, inducing clockwise rotation and an increase in θ (region B). Simultaneously, the gradient of d reverses. When the rod stops rotating (region C), it extends toward the bottom-right, and the resulting torque again drives rotational motion. Additionally, the $d-\theta$ plots indicate that the oscillatory dynamics form a limit cycle (Fig. S5b [28]).

Figure 4 illustrates the V_p -dependence of the oscillation for an $l = 80$ μm rod. The temporal evolution of θ (Fig. 4a) exhibits relatively stable oscillation with minor fluctuations in amplitude and period. As V_p increases, the period decreases, whereas the amplitude increases. This trend is quantified in Fig. 4b, where the angular amplitude A_θ increases and the period p_θ decreases with increasing V_p (see also Fig. S5b [28]). Both quantities are history-independent and determined solely by V_p, as demonstrated by the nonmonotonic voltage sequence in Fig. 4b (see also Fig. S6 and Table S1 [28]).

Several factors may contribute to the observed oscillation. First, as the rod orientation changes, the surrounding ICEO flow field may respond with a delay (cf. Fig. S1 [28]), producing asymmetry in the flow field and thereby coupling translational and rotational motion. Second, at sufficiently high V_p, we observed that one end of an oscillating rod slightly lifted off the surface. Considering the arched shape of long rods, such out-of-plane deviations from strictly two-dimensional motion may also influence oscillatory dynamics. To elucidate the underlying

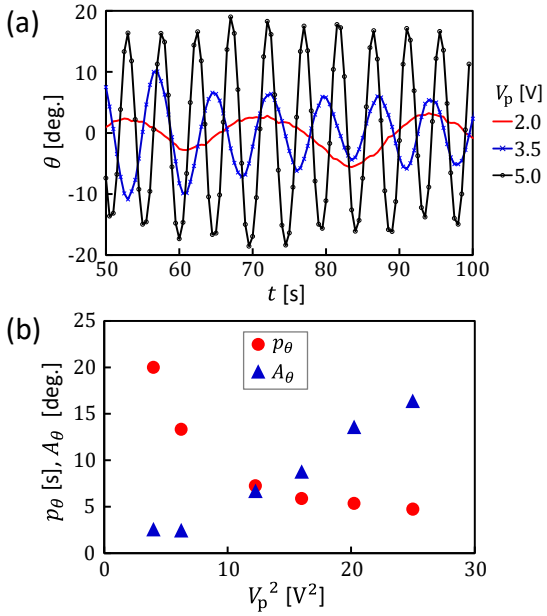

FIG 4. V_p-dependence of self-excited oscillation of an $l = 80$ μm rod. (a) Temporal evolution of θ at three representative voltage amplitudes: 2.0 V (red line), 3.5 V (blue crosses with line), and 5.0 V (black open circles with line). $t = 0$ indicates the time at which V_p was changed. (b) Angular oscillation amplitude (A_θ), averaged over observation periods exceeding 90 s , and oscillation period (p_θ), obtained from the peak frequency of the Fourier transformation of $\theta(t)$. V_p was changed sequentially as 2.0, 2.5, 4.0, 4.5, 3.5, 5.0 V.

mechanism, further studies are needed, including flow-field analysis using particle image velocimetry (PIV). Such measurements would directly clarify the origin of the rotation–translation coupling in the self-excited oscillation and provide insight into the reorientation processes and short-time dynamics described in Sec. A and S2 [28].

IV. CONCLUSIONS

We demonstrated that long rectangular dielectric rods with a thin metal layer along their long axis exhibit unique self-propulsive motion *via* induced-charge electrophoresis. Their translational behavior undergoes a discontinuous transition between horizontal and vertical modes depending on the applied electric field strength. These two modes exhibit bistability, with both the velocity contrast and the bistable voltage range increasing with rod length. Additionally, long rods in the horizontal mode become *confined* by small obstacles through their own propulsion and subsequently exhibit self-excited oscillations.

These distinct behaviors arise primarily from the rods' pronounced uniaxial shape anisotropy, which lies perpendicular to the propulsion direction. The vertical mode is stabilized by field-induced torque, while the horizontal mode is favored by gravitational potential, qualitatively explaining the bistability. The large difference in effective rod length parallel to the electric field between the two modes significantly modifies the ICEO slip velocity, leading to the observed speed disparity. Self-entrapment, in turn, emerges from shape-induced torque resulting from the asymmetry in rods' arm length upon collision.

Our study demonstrates a clear coupling between particle structure (large uniaxial anisotropy and Janus symmetry), the resulting force balance (field-induced and gravitational forces), and emergent dynamics (translational mode transition, self-entrapment, and oscillation). This structure–property–function cascade highlights new design principles for active matter and microscale engineering. More sophisticated control of swimmer dynamics may be achieved by introducing multi-axis geometric anisotropy or applying additional external fields, such as magnetic fields, thereby inducing further distinctive nonlinear behaviors [50, 51]. More broadly, anisotropy-driven properties and functionalities provide a versatile platform for exploring collective phenomena in active matter and may be harnessed for applications in particle transport, fluid mixing, and energy harvesting in microfluidic and MEMS devices. Shape thus emerges as a fundamental design parameter for enhancing the intelligence and functionality of micro-agents.

ACKNOWLEDGMENTS

The authors thank Natsumi Eto (Kyushu University) and Taiga Sato (Kyoto Sangyo University) for their contributions to the preliminary experiments. They also thank Masatoshi Ichikawa (Hiroshima University) for fruitful discussions. Y.I. gratefully acknowledges financial support from JSPS KAKENHI (Grant No. 20H01876).

Author Contributions

All authors designed the research. Y.I. conducted the experiments and analyzed the data. All authors wrote the manuscript and have given approval to the final version of the manuscript.

[1] C. Bechinger, R. Di Leonardo, H. Löwen, C. Reichhardt, G. Volpe, and G. Volpe, Active particles in complex and crowded environments, *Rev. Mod. Phys.* **88**, 045006 (2016).

[2] K. J. Bishop, S. L. Biswal, and B. Bharti, Active colloids as models, materials, and machines, *Annu. Rev. Chem. Biomol. Eng.* **14**, 1 (2023).

[3] A. I. Bunea, D. Martella, S. Nocentini, C. Parmeggiani, R. Taboryski, and D. S. Wiersma, Light-powered microrobots: Challenges and opportunities for hard and soft responsive microswimmers, *Adv. Intell. Syst.* **3**, 2000256 (2021).

[4] S. R. Dabbagh, M. R. Sarabi, M. T. Birtek, S. Seyfi, M. Sitti, and S. Tasoglu, 3D-printed microrobots from design to translation, *Nat. Commun.* **13**, 5875 (2022).

[5] D. Nishiguchi and M. Sano, Mesoscopic turbulence and local order in Janus particles self-propelling under an AC electric field, *Phys. Rev. E* **92**, 052309 (2015).

[6] J. Yan, M. Han, J. Zhang, C. Xu, E. Luijten, and S. Granick, Reconfiguring active particles by electrostatic imbalance, *Nat. Mater.* **15**, 1095 (2016).

[7] K. Saito, R. Kawano, C. Sadamatsu, Y. Iwashita, and Y. Kimura, Self-propelled motion of induced-charge electrophoretic Janus particles in viscoelastic fluids, *Phys. Rev. E* **111**, 045409 (2025).

[8] C. W. Shields IV, K. Han, F. Ma, T. Miloh, G. Yossifon, and O. D. Velev, Supercolloidal spinners: Complex active particles for electrically powered and switchable rotation, *Adv. Funct. Mater.* **28**, 1803465 (2018).

[9] A. Al Harraq, R. Patel, J. G. Lee, O. Owoyele, J. Chun, and B. Bharti, Non-Reciprocity, Metastability, and Dynamic Reconfiguration in Co-Assembly of Active and Passive Particles, *Advanced Science*, **12**, 2409489 (2025).

[10] S. E. Moran, I. R. Bruss, P. W. A. Schönhöfer, and S. C. Glotzer,Particle anisotropy tunes emergent behavior in active colloidal systems, *Soft Matter* **18**, 1044 (2022).

[11] S. E. Moran, P. W. A. Schönhöfer, and S. C. Glotzer, Shape-driven, emergent behavior in active particle mixtures, *New J. Phys.* **24**, 063007 (2022).

[12] H. Ebata, A. Yamamoto, Y. Tsuji, S. Sasaki, K. Moriyama, T. Kuboki, and S. Kidoaki, Persistent random deformation model of cells crawling on a gel surface, *Sci. Rep.* **8**, 5153 (2018).

[13] O. Shemi and M. J. Solomon, Self-propulsion and active motion of Janus ellipsoids, *J. Phys. Chem. B* **122**, 10247 (2018).

[14] D. Nicholls, A. DeVerse, R. S. Esplin, J. Castañeda, Y. Loyd, R. Nair, and J. G. Gibbs, Shape-dependent motion of structured

photoactive microswimmers, *ACS Appl. Mater. Interfaces* **10**, 18050 (2018).
[15] R. P. Doherty, T. Varkevisser, M. Teunisse, J. Hoecht, S. Ketzetzi, S. Ouhajji, and D. J. Kraft, Catalytically propelled 3D printed colloidal microswimmers, *Soft Matter* **16**, 10463 (2020).
[16] J. Katuri, R. Poehnl, A. Sokolov, W. Uspal, and A. Snezhko, Arrested-motility states in populations of shape-anisotropic active Janus particles, *Sci. Adv.* **8**, eabo3604 (2022).
[17] S. K. Panda, S. Debata, N. A. Kherani, and D. P. Singh, Dynamics and phase behavior of metallo-dielectric rod-shaped microswimmers driven by alternating current electric field, *Soft Matter* **20**, 3971 (2024).
[18] G. Anchutkin, F. Cichos, and V. Holubec, Run-and-tumble motion of ellipsoidal microswimmers, *Phys. Rev. Res.* **6**, 043101 (2024).
[19] S. Badaire, C. Cottin-Bizonne, J. W. Woody, A. Yang, and A. D. Stroock, Shape selectivity in the assembly of lithographically designed colloidal particles, *J. Am. Chem. Soc.* **129**, 40 (2007).
[20] R. Koike, Y. Iwashita, and Y. Kimura, Emulsion droplets stabilized by close-packed Janus regular polygonal particles, *Langmuir* **34**, 12394 (2018).
[21] T. M. Squires and M. Z. Bazant, Induced-charge electro-osmosis, *J. Fluid Mech.* **509**, 217 (2004).
[22] T. M. Squires and M. Z. Bazant, Breaking symmetries in induced-charge electro-osmosis and electrophoresis, *J. Fluid Mech.* **560**, 65 (2006).
[23] S. Gangwal, O. J. Cayre, M. Z. Bazant, and O. D. Velev, Induced-charge electrophoresis of metallodielectric particles, *Phys. Rev. Lett.* **100**, 058302 (2008).
[24] H. H. Wensink and H. Löwen, Emergent states in dense systems of active rods: From swarming to turbulence, *J. Phys.: Condens. Matter* **24**, 464130 (2012).
[25] H. H. Wensink, J. Dunkel, S. Heidenreich, K. Drescher, R. E. Goldstein, H. Löwen, and J. M. Yeomans, Meso-scale turbulence in living fluids, *Proc. Natl. Acad. Sci. U.S.A.* **109**, 14308 (2012).
[26] A. Doostmohammadi, J. Ignés-Mullol, J. M. Yeomans, and F. Sagués, Active nematics. *Nature communications*, **9**, 3246 (2018).
[27] M. Bär, R. Großmann, S. Heidenreich, and F. Peruani, Self-propelled rods: Insights and perspectives for active matter, *Annu. Rev. Condens. Matter Phys.* **11**, 441 (2020).
[28] See Supplemental Material [url], which includes Refs. [29-31].
[29] W. S. Rasband, *ImageJ*, U.S. National Institutes of Health, Bethesda, MD (1997–2012).
[30] The Chemical Society of Japan, *Handbook of Chemistry: Pure Chemistry*, 6th ed. (Maruzen-Publishing, Tokyo, 2021).
[31] J. N. Israelachvili, *Intermolecular and Surface Forces*, 3rd ed. (Elsevier, New York, 2011), p. 263.
[32] J. J. Arcenegui, P. García-Sánchez, H. Morgan, and A. Ramos, Electro-orientation and electrorotation of metal nanowires, *Phys. Rev. E* **88**, 063018 (2013).
[33] J. E. Flores-Mena, P. García-Sánchez, and A. Ramos, Electrokinetics of metal cylinders, *Phys. Rev. E* **99**, 032603 (2019).
[34] H. Feng, H. Chang, X. Zhong, and T. N. Wong, Recent advancement in induced-charge electrokinetic phenomena and their micro- and nano-fluidic applications, *Adv. Colloid Interface Sci.* **280**, 102159 (2020).
[35] M. Z. Bazant, M. S. Kilic, B. D. Storey, and A. Ajdari, Nonlinear electrokinetics at large applied voltages, arXiv:cond-mat/0703035 (2007).
[36] M. Z. Bazant, M. S. Kilic, B. D. Storey, and A. Ajdari, Towards an understanding of induced-charge electrokinetics at large applied voltages in concentrated solutions, *Adv. Colloid Interface Sci.* **152**, 48 (2009).
[37] J. S. Paustian, A. J. Pascall, N. M. Wilson, and T. M. Squires, Induced charge electroosmosis micropumps using arrays of Janus micropillars, *Lab Chip* **14**, 3300 (2014).
[38] A. Boymelgreen, G. Yossifon, and T. Miloh, Propulsion of active colloids by self-induced field gradients, *Langmuir* **32**, 9540 (2016).
[39] S. Wang, Y. Chen, X. Zhou, L. Lei, Z. H. Shah, G. Lin, and Y. Gao, Magnetic manipulation and assembly of nonmagnetic colloidal rods in a ferrofluid. *Langmuir*, **37**, 1429 (2021).
[40] K. Beppu, and J. V. I. Timonen, Magnetically controlled bacterial turbulence, *Commun. Phys.* **7**, 216 (2024).